Comput. Mech. (2006) 38: 235–249
DOI 10.1007/s00466-005-0744-8

ORIGINAL PAPER

D. C. Simkins · S. Li

Meshfree simulations of thermo-mechanical ductile fracture

Received: 23 January 2004 / Accepted: 21 July 2005 / Published online: 25 November 2005

Abstract In this work, a meshfree method is used to simulate thermo-mechanical ductile fracture under finite deformation. A Galerkin meshfree formulation incorporating the Johnson-Cook damage model is implemented in numerical computations. We are interested in the simulation of thermo-mechanical effects on ductile fracture under large scale yielding. A rate form adiabatic split is proposed in the constitutive update. Meshfree techniques, such as the visibility criterion, are used to modify the particle connectivity based on evolving crack surface morphology. The numerical results have shown that the proposed meshfree algorithm works well, the meshfree crack adaptivity and re-interpolation procedure is versatile in numerical simulations, and it enables us to predict thermo-mechanical effects on ductile fracture.

Keywords Damage · Ductile Fracture · Johnson-Cook model · Meshfree method · Thermo-mechanical coupling

1 Introduction

A main application of meshfree methods is computational fracture mechanics, or computational failure mechanics. In the early 1990s, Belytschko and his co-workers [4,5,19] showed that meshfree discretization and interpolation have the flexibility to adapt to the change of the geometrical or topological structure of a solid due to fracture, and therefore it is advantageous to employ meshfree methods when simulating crack growth and crack propagation, which can otherwise be a painful process when using a finite element adaptive process, such as remeshing, in crack simulations e.g., [27].

D. C. Simkins
Department of Civil and Environmental Engineering,
University of South Florida,
Tampa, FL 33620, USA

S. Li (✉)
Department of Civil and Environmental Engineering,
University of California,
Berkeley, CA 94720, USA
E-mail: li@ce.berkeley.edu

Recently, there have been quite a few works using meshfree or meshfree related methods simulating fracture problems, such as Krysl and Belytschko [16,17], Daux et al. [11], Dolbow et al. [12], Stolarska et al. [25], and Ventura et al. [26]. Another alternative is the so-called cohesive finite element method (FEM) e.g., [21,31]. The cohesive FEM may avoid remeshing, but it has severe limitations: such as mesh dependence and limitations on embedding complex constitutive relations. For instance, cohesive FEM has great difficulties in modeling ductile fracture at large scale yielding, and ductile fracture under combined thermo-mechanical loading, because a realistic interfacial cohesive thermal-mechanical constitutive relation is still lacking.

One of the main features of ductile fracture is its dissipative character, because a large amount of heat generated by plastic work around the crack tip area will cause additional thermal softening and thermal damage, which in turn will affect ductile crack growth. To the best of the authors' knowledge, we haven't seen any interfacial cohesive model in the open literature that is capable to deal with thermo-mechanical effects in the ductile fracture. It is the main purpose and motivation of this paper to demonstrate the ability of meshfree methods to deal with thermo-mechanical ductile fracture.

The main technical difficulties in simulating thermo-mechanical effects in ductile fracture are:

(1) how to implement a stable constitutive update to handle the thermo-mechanical coupling during crack propagation, and
(2) how to simulate crack growth without impairing the original interpolation field.

The first difficulty emerges when thermal softening is coupled with heat conduction. This will create a nonlinear coupled system with complex stability behavior. The situation becomes even more complicated when it is associated with large scale yielding, finite deformation, and evolving configuration (crack growth).

The second difficulty is more serious. Because ductile fracture is an irreversible process, the history of state variables, such as temperature, damage, plastic strain and yield stress,

at each material point, e.g., a Gauss point in a computation domain, have to be preserved in a bookkeeping process at each time step.

If the original mesh can not automatically adapt to arbitrary crack paths, any remeshing process will need to map or convert state variables from the old interpolation field to the new interpolation field, which is not only a time consuming process but also a major source of accumulated numerical error that eventually prohibits any possible realistic long term simulation.

The objective of this study is to provide a simple but relatively accurate and yet cost effective solution that may lead to the final solution of this outstanding problem in computational fracture mechanics.

To achieve this objective, we use meshfree interpolation to approximate the discretized fields. We adopt the Johnson-Cook model in constitutive modeling and in damage assessment. To model surface separation, we use a newly designed parametric visibility condition and its related particle splitting algorithm to modify the previous interpolation and connectivity map among meshfree particles.

The paper is organized into five sections. In Sect. 2, we discuss the basic meshfree formulation, in which a rate form operator splitting algorithm is proposed for the constitutive update. In Sect. 3, we shall briefly outline a parametric visibility condition and its related particle splitting algorithm, and how to use them in ductile crack surface modeling. Numerical examples are presented in Sect. 4. A few remarks are made in the last section.

2 Meshfree Formulations

2.1 Thermo-mechanical couplings

In this work, we are mainly interested in ductile fracture induced by damage during a thermo-mechanical process. The ensuing meshfree simulation considers a fully coupled thermo-mechanical system.

By the dynamic principle of virtual power, we have the following weak formulation,

$$\int_V \boldsymbol{\tau} : \delta\mathbf{d}\, \mathrm{d}V = \int_{\Gamma_t} \mathbf{t}\cdot\delta\mathbf{v}\, \mathrm{d}S - \int_V \rho\frac{\partial^2\mathbf{u}}{\partial t^2}\cdot\delta\mathbf{v}\, \mathrm{d}V\,, \tag{2.1}$$

where V is the volume of the solid, Γ_t is the part of the surface ∂V upon which the traction, $\mathbf{t}$, is prescribed, $\boldsymbol{\tau}$ is the Kirchhoff stress, $\mathbf{u}$ is the displacement, $\mathbf{v}$ is the velocity, $\mathbf{d} := \frac{1}{2}(grad\mathbf{v} + grad^{\mathrm{T}}\mathbf{v})$ is the rate of deformation, and ρ is the material density.

The variational weak form of the energy equation in the context of large deformation is,

$$\begin{aligned}\int_V \rho C_p\frac{\partial T}{\partial t}\delta T\, \mathrm{d}V &= \int_V \chi\boldsymbol{\tau} : \mathbf{d}^p\delta T\, \mathrm{d}V \\ &+ \int_{\partial V}\left(\mathbf{F}^{-1}\cdot\mathbf{K}\cdot\mathbf{F}^{-\mathrm{T}}\cdot\nabla T\right)\cdot\mathbf{N}\delta T\, \mathrm{d}S \\ &- \int_V \left(\mathbf{F}^{-1}\cdot\mathbf{K}\cdot\mathbf{F}^{-T}\cdot\nabla T\right)\cdot\nabla\delta T\, \mathrm{d}V\,,\end{aligned} \tag{2.2}$$

where $\mathbf{F}$ is the deformation gradient, T is the temperature (K^{o}), $\mathbf{N}$ is the outward-normal of the surface ∂V, t is time, χ denotes the fraction of plastic work converted to heat, $\mathbf{d}^p$ is the plastic rate of deformation, C_p is the specific heat. For isotropic is heat conduction, the heat conductivity tensor $\mathbf{K} = \kappa\mathbf{1}^{(2)}$, where κ is the heat condutivity coefficient, $\mathbf{1}^{(2)}$ is the second order unit tensor, ∇ is the gradient operator in the reference configuration, superscripts $^{-1}$ and $^{\mathrm{T}}$ denote the inverse and transpose of a tensor, and δT, $\delta\mathbf{d}$ and $\delta\mathbf{v}$ denote admissible variations in temperature, rate of deformation, and velocity, respectively.

The strong form of the linear momentum balance is,

$$\nabla\cdot\mathbf{P} = \rho_0\frac{\partial^2\mathbf{u}}{\partial t^2} \tag{2.3}$$

and the strong form of energy balance is

$$\rho_0 C_p\frac{\partial T}{\partial t} = \chi\boldsymbol{\tau} : \mathbf{d}^p + \nabla\Big(J\mathbf{F}^{-1}\cdot\mathbf{K}\cdot\mathbf{F}^{-\mathrm{T}}\cdot\nabla T\Big) \tag{2.4}$$

These two equations are coupled intrinsically through the constitutive equations. Consider the rate form constitutive model. We decompose the rate-of-deformation tensor $\mathbf{d}$ additively into elastic, plastic, and thermal parts,

$$\mathbf{d} = \mathbf{d}^e + \mathbf{d}^p + \mathbf{d}^{\mathrm{T}} \tag{2.5}$$

where the superscripts, e, p, and T, denote the elastic, plastic (or inelastic), and thermal rate of deformation respectively.

The Jaumann rate of the Kirchhoff stress is used in the rate form hypo-elastic formulation, i.e.,

$$\boldsymbol{\tau}^{\nabla J} = \mathbf{C} : \mathbf{d}^e = \mathbf{C} : (\mathbf{d} - \mathbf{d}^p - \mathbf{d}^{\mathrm{T}}) \tag{2.6}$$

where the Jaumann rate of the Kirchhoff stress is defined as

$$\boldsymbol{\tau}^{\nabla J} := \dot{\boldsymbol{\tau}} - \mathbf{W}\cdot\boldsymbol{\tau} + \boldsymbol{\tau}\cdot\mathbf{W}, \tag{2.7}$$

with $\{\cdot\} = \dfrac{\mathrm{d}}{\mathrm{d}t}\{\ \}$. The elastic tensor is isotropic,

$$C_{ijk\ell} = \Big(K - \frac{2}{3}G\Big)\delta_{ij}\delta_{k\ell} + G(\delta_{ik}\delta_{j\ell} + \delta_{i\ell}\delta_{jk}) \tag{2.8}$$

and the bulk and shear moduli can be linked to Young's modulus and Poisson's ratio by

$$G = \frac{E}{2(1+\nu)} \tag{2.9}$$

$$K = \frac{E}{3(1-2\nu)} \tag{2.10}$$

The rate of deformation due to thermal stress and plasticity are

$$\begin{aligned}\mathbf{d}^{\mathrm{T}} &= \alpha\dot{T}\mathbf{1}^{(2)} \\ \mathbf{d}^{\mathbf{p}} &= \dot{\bar{\epsilon}}\hat{n}.\end{aligned} \tag{2.11}$$

The rate form constitutive relation is

$$\boldsymbol{\tau}^{\nabla J} = \mathbf{C} : \Big(\mathbf{d} - \dot{\bar{\epsilon}}\hat{\mathbf{n}} - \alpha\dot{T}\mathbf{1}^{(2)}\Big). \tag{2.12}$$

In general, the numerical simulation of such coupled thermo-mechanical systems is complex and difficult, for example, Zhou et al. [33]. This is because a coupled

thermo-mechanical system usually involves different time scales associated with the thermal and mechanical fields. An effective numerical integration scheme to solve the fully-coupled energy equation is the so-called operator splitting technique, which was proposed by Armero and Simo in the early 1990s [1,2] in the context of hyperelastic/multiplicative decomposition based thermoplastic solids. In Armero and Simo [1,2], they decoupled the thermo-mechanical system into two sub-systems: an adiabatic mechanical system and heat conduction based thermal system. By doing this, one can obtain a stable and effective integration algorithm based on operator splitting.

Following the same philosophy, in this work, we extend this strategy to the thermo-mechanical solid that obeys a rate form constitutive law under finite deformation and irreversible damage.

The energy balance may be split into two parts:

(a) heat generation due to plastic deformation, and
(b) heat conduction. Thus, the energy balance may be divided into two steps:

$$\begin{cases} \text{Adiabatic heating:} \quad \rho_0 C_p \dfrac{\partial T}{\partial t} = \chi\, \boldsymbol{\tau} : \mathbf{d}^p; \\ \text{Heat conduction:} \quad \rho_0 C_p \dfrac{\partial T}{\partial t} = \nabla\Big(J\mathbf{F}^{-1}\cdot\mathbf{K}\cdot\mathbf{F}^{-\mathrm{T}}\cdot\nabla T\Big) \end{cases} \tag{2.13}$$

The integration of the energy equation consists of two steps:

(1) we proceed with the temperature update due to adiabatic heating in the constitutive update loop, and
(2) we update the temperature change due to heat conduction in the main integration loop by only considering the following weak form,

$$\int_V \rho_0 C_p \frac{\partial T}{\partial t}\delta T \,\mathrm{d}V = \int_{\partial V}\Big(\mathbf{F}^{-1}\cdot\mathbf{K}\cdot\mathbf{F}^{-\mathrm{T}}\cdot\nabla T\Big)\cdot\mathbf{N}\delta T \,\mathrm{d}S - \int_V \kappa\Big(\mathbf{F}^{-1}\cdot\mathbf{K}\cdot\mathbf{F}^{-\mathrm{T}}\cdot\nabla T\Big)\cdot\nabla\delta T \,\mathrm{d}V. \tag{2.14}$$

Introducing a meshfree discretization, the primary fields can be approximated as

$$\mathbf{u}^h(\mathbf{X},t) = \sum_{i=1}^{\mathrm{np}} N_i(\mathbf{X})\mathbf{U}_i(t), \quad \text{with } \mathbf{U}_i(t) = \{U_{i1}, U_{i2}, U_{i3}\}^{\mathrm{T}} \tag{2.15}$$

$$\delta\mathbf{v}^h(\mathbf{X},t) = \sum_{i=1}^{\mathrm{np}} N_i(\mathbf{X})\delta\mathbf{V}_i(t), \quad \text{with } \delta\mathbf{V}_i(t) = \{V_{i1}, V_{i2}, V_{i3}\}^{\mathrm{T}} \tag{2.16}$$

$$T^h(\mathbf{X},t) = \sum_{i=1}^{\mathrm{np}} N_i(\mathbf{X})T_i(t), \quad \text{and } \delta T^h(\mathbf{X},t) = \sum_{i=1}^{np} N_i(\mathbf{X})\delta T_i(t), \tag{2.17}$$

Let

$$\mathbf{U}(t) = \{\mathbf{U}_1, \mathbf{U}_2, \ldots\ldots, \mathbf{U}_{\mathrm{np}}\}^{\mathrm{T}} \tag{2.18}$$

$$\mathbf{T}(t) = \{T_1, T_2, \ldots\ldots, T_{\mathrm{np}}\}^{\mathrm{T}}. \tag{2.19}$$

Then the weak formulations (2.1) and (2.14) can be reduced to the following algebraic equations,

$$\mathbf{M}\cdot\frac{d^2\mathbf{U}}{dt^2} = \mathbf{f}_{\mathrm{ext}} - \mathbf{f}_{\mathrm{int}}, \tag{2.20}$$

$$\mathbf{C}\cdot\frac{d\mathbf{T}}{dt} = -\mathbf{H}\cdot\mathbf{T}, \tag{2.21}$$

where the mass matrix, $\mathbf{M} = \{M_{ij}\}$ is defined as

$$M_{ij} = \int_V \rho_0 N_i(\mathbf{X}) N_j(\mathbf{X}) \,\mathrm{d}V, \tag{2.22}$$

and the thermal capacitance and conductivity matrices, $\mathbf{C}$ and $\mathbf{H}$, are defined as

$$\mathbf{C} = [C_{ij}], \quad C_{ij} := \int_{\Omega_X} \rho_0 C_p N_i(\mathbf{X}) N_j(\mathbf{X}) \,\mathrm{d}\Omega_X \tag{2.23}$$

$$\mathbf{H} = [H_{ij}], \quad H_{ij} := \int_{\Omega_X} \kappa F^{-1}_{I\ell}(\mathbf{X}) F^{-\mathrm{T}}_{\ell J}(\mathbf{X}) N_{i,J}(\mathbf{X}) N_{j,I}(\mathbf{X}) \,\mathrm{d}\Omega_X \tag{2.24}$$

The internal and external force vectors in (2.20) are defined as

$$\mathbf{f}^{\mathrm{int}} = \{\mathbf{f}_1^{\mathrm{int}}, \mathbf{f}_2^{\mathrm{int}}, \ldots\ldots, \mathbf{f}_{\mathrm{np}}^{\mathrm{int}}\}^T, \quad \text{and } \mathbf{f}_i^{\mathrm{int}} = \int_{\Omega_X} P_{\ell J}\frac{\partial N_i}{\partial X_J}\mathbf{e}_\ell \,\mathrm{d}\Omega_X \tag{2.25}$$

$$\mathbf{f}^{\mathrm{ext}} = \{\mathbf{f}_1^{\mathrm{ext}}, \mathbf{f}_2^{\mathrm{ext}}, \ldots\ldots, \mathbf{f}_{\mathrm{np}}^{\mathrm{ext}}\}^{\mathrm{T}}, \quad \text{and } \mathbf{f}_i^{\mathrm{ext}} = \int_{\Gamma_t} T^0_\ell(\mathbf{X},t) N_i(\mathbf{X})\mathbf{e}_\ell \,\mathrm{d}S \tag{2.26}$$

where $\mathbf{e}_\ell$ are the basis vectors of the Cartesian coordinate.

The inelastic solid is assumed to undergo finite deformations, with the total deformation gradient denoted as $\mathbf{F}$. The rate of deformation tensor, $\mathbf{d}$, and the spin tensor, $\mathbf{W}$, are the symmetric and anti-symmetric parts of the spatial velocity gradient $\mathbf{l} = \dot{\mathbf{F}}\cdot\mathbf{F}^{-1}$, i.e.,

$$\mathbf{d} + \mathbf{W} = \dot{\mathbf{F}}\cdot\mathbf{F}^{-1} \tag{2.27}$$

and

$$\mathbf{d} := d_{ij}\mathbf{e}_i\otimes\mathbf{e}_j, \quad d_{ij} := \frac{1}{2}\Big(\frac{\partial v_i}{\partial x_j} + \frac{\partial v_j}{\partial x_i}\Big) \tag{2.28}$$

$$\mathbf{W} := W_{ij}\mathbf{e}_i\otimes\mathbf{e}_j, \quad W_{ij} := \frac{1}{2}\Big(\frac{\partial v_i}{\partial x_j} - \frac{\partial v_j}{\partial x_i}\Big) \tag{2.29}$$

where v_i are the velocity components.

2.2 The Johnson-Cook model

To model the thermo-mechanical effects of ductile fracture, we choose a well calibrated constitutive model—the Johnson-Cook model, which has been extensively used in ductile failure analysis, e.g., Johnson & Cook [14, 15], Batra & Chen [3], among others.

Define the hydrostatic, deviatoric, and equivalent stresses as

$$\tau_m = \frac{1}{3}\boldsymbol{\tau} : \mathbf{1}^{(2)} \tag{2.30}$$

$$\mathbf{s} = \boldsymbol{\tau} - \tau_m \mathbf{1}^{(2)} \tag{2.31}$$

$$\tau_{\text{eq}} = \left(\frac{3}{2}\mathbf{s} : \mathbf{s}\right)^{1/2} \tag{2.32}$$

The plastic rate of deformation is obtained from the following flow rule,

$$\mathbf{d}^p = \dot{\bar{\epsilon}}\hat{\mathbf{n}} \tag{2.33}$$

where

$$\hat{\mathbf{n}} := \frac{3}{2\tau_{\text{eq}}}\mathbf{s} \tag{2.34}$$

and

$$\dot{\bar{\epsilon}} = \dot{\epsilon}_0 \exp\left\{\frac{1}{C}\left(\frac{\bar{\tau}_Y}{g(\bar{\epsilon}, T)} - 1\right)\right\}. \tag{2.35}$$

In Eq. (2.35), the parameter $\bar{\tau}_Y$ is the initial yield stress, and the non-dimensional function,

$$g(\bar{\epsilon}, T) = \left[A + B\bar{\epsilon}^n\right][1 - \mathcal{T}^m], \quad \text{with,} \quad \mathcal{T} = \frac{T - T_{\text{room}}}{T_{\text{melt}} - T_{\text{room}}}. \tag{2.36}$$

where T_{room} is the room temperature, T_{melt} is the melting temperature.

Fracture of Johnson-Cook solids occurs when a damage measure reaches one, i.e., $D = 1$, which is calculated according to the following cumulative damage law:

$$D = \sum \frac{\Delta\epsilon}{\epsilon_f} \tag{2.37}$$

where

$$\epsilon_f = \left[D_1 + D_2 \exp(D_3 \frac{\tau_m}{\bar{\tau}_Y})\right]\left[1 + D_4 \ln \dot{\epsilon}\right][1 + D_5\mathcal{T}]. \tag{2.38}$$

where $\tau_m = \frac{1}{3}(\tau_{11} + \tau_{22} + \tau_{33})$.

2.3 Constitutive update

In this section, we discuss how to update the Kirchhoff stress and temperature due to adiabatic heating.

The Kirchhoff stress update is based on the following improved Euler scheme [22],

$$\begin{aligned}\boldsymbol{\tau}_{n+1} &= \boldsymbol{\tau}_n + \Delta\boldsymbol{\tau} \\ &= \boldsymbol{\tau}_n + \dot{\boldsymbol{\tau}}_\theta \Delta t\,,\end{aligned} \tag{2.39}$$

and

$$\dot{\boldsymbol{\tau}}_\theta \approx \boldsymbol{\tau}_\theta^{\nabla J} + \mathbf{W}_n \cdot \boldsymbol{\tau}_n - \boldsymbol{\tau}_n \cdot \mathbf{W}_n^T, \tag{2.40}$$

where $\boldsymbol{\tau}_\theta \in [\boldsymbol{\tau}_t, \boldsymbol{\tau}_{t+\Delta t}]$ and $\dot{\boldsymbol{\tau}}_\theta \in [\dot{\boldsymbol{\tau}}_t, \dot{\boldsymbol{\tau}}_{t+\Delta t}]$.

The first step is to find $\boldsymbol{\tau}_\theta^{\nabla J}$ via,

$$\boldsymbol{\tau}_\theta^{\nabla J} = \mathbf{C} : \left(\mathbf{d}_\theta - \dot{\bar{\epsilon}}_\theta \hat{\mathbf{n}}_\theta - \alpha \dot{T}_\theta \mathbf{I} \otimes \mathbf{I}\right). \tag{2.41}$$

The crucial step is how to determine $\dot{\bar{\epsilon}}_\theta$. By definition

$$\Delta\bar{\epsilon} = \Delta t[(1-\theta)\dot{\bar{\epsilon}}_n + \theta\dot{\bar{\epsilon}}_{n+1}] = \dot{\bar{\epsilon}}_\theta \Delta t, \quad \rightarrow \quad \dot{\bar{\epsilon}}_\theta = \frac{\Delta\bar{\epsilon}}{\Delta t}. \tag{2.42}$$

By Taylor expansion

$$\Delta\bar{\epsilon} = \dot{\bar{\epsilon}}_t \Delta t + \theta(\Delta t)^2\left[\frac{\partial\dot{\bar{\epsilon}}}{\partial\bar{\epsilon}}\Big|_t \dot{\bar{\epsilon}}_\theta + \frac{\partial\dot{\bar{\epsilon}}}{\partial\bar{\tau}_Y}\Big|_t \dot{\bar{\tau}}_{Y\theta} + \frac{\partial\dot{\bar{\epsilon}}}{\partial T}\Big|_t \dot{T}_\theta\right] + \mathcal{O}\left(\Delta t^3\right), \tag{2.43}$$

where

$$\frac{\partial\dot{\bar{\epsilon}}}{\partial\bar{\epsilon}} = \dot{\epsilon}_0 \exp\left\{\frac{1}{C}\left(\frac{\bar{\tau}_Y}{g(\bar{\epsilon}, T)} - 1\right)\right\}\left\{-\frac{1}{C}\frac{\bar{\tau}_Y}{g^2(\bar{\epsilon}, T)}\right\}\left(\frac{\partial g}{\partial\bar{\epsilon}}\right) \tag{2.44}$$

$$\frac{\partial g}{\partial\bar{\epsilon}} = Bn\bar{\epsilon}^{-(n-1)}\left(1 - \mathcal{T}^m\right), \tag{2.45}$$

$$\frac{\partial\dot{\bar{\epsilon}}}{\partial\bar{\tau}_Y} = \frac{\dot{\bar{\epsilon}}}{Cg(\bar{\epsilon}, T)}, \tag{2.46}$$

$$\frac{\partial\dot{\bar{\epsilon}}}{\partial T} = \left(-\frac{\dot{\bar{\epsilon}}\ \bar{\tau}_Y}{Cg^2(\bar{\epsilon}, T)}\right)\left(\frac{\partial g}{\partial T}\right), \tag{2.47}$$

$$\frac{\partial g}{\partial T} = -\frac{m\mathcal{T}^{m-1}}{(1 - \mathcal{T}^m)(T_{\text{melt}} - T_{\text{room}})} g(\bar{\epsilon}, T) \tag{2.48}$$

The next step is to evaluate $\dot{\tau}_{\text{eq}\theta}$ at $t_\theta \in [t, t + \Delta t]$ or $[t_n, t_{n+1}]$.

By definition,

$$\tau_{\text{eq}\theta} = \left(\frac{3}{2}\mathbf{s}_\theta : \mathbf{s}_\theta\right)^{1/2}.$$

In large deformation,

$$\dot{\tau}_{\text{eq}\theta} = \frac{3}{2\bar{\tau}_{Y\theta}}\mathbf{s}_\theta : \boldsymbol{\tau}^{\nabla J} \tag{2.49}$$

Considering

$$\mathbf{n}_\theta = \frac{3}{2\bar{\tau}_{Y\theta}}\mathbf{s}_\theta \tag{2.50}$$

and adiabatic heating,

$$\dot{T}_\theta = \frac{\chi}{\rho C_p}\tau_{\text{eq}\theta}\dot{\bar{\epsilon}}_\theta, \tag{2.51}$$

we have

$$\begin{aligned}\dot{\tau}_{\text{eq}\theta} &= \mathbf{n}_\theta : \left\{\mathbf{C} : \left(\mathbf{d}_\theta - \mathbf{d}_\theta^p - \mathbf{d}^T\right)\right\} \\ &= \mathbf{n}_\theta : \left\{\mathbf{C} : \mathbf{d}_\theta - \dot{\bar{\epsilon}}_\theta \mathbf{C} : \mathbf{n}_\theta - \frac{\alpha\chi}{\rho C_\rho}\left(\mathbf{C} : \mathbf{1}^{(2)}\right)\left(\boldsymbol{\tau}_\theta : \mathbf{d}_\theta^p\right)\right\}.\end{aligned} \tag{2.52}$$

Noting

$$\mathbf{C} : \mathbf{1}^{(2)} = 3K\mathbf{1}^{(2)}, \text{ and } \boldsymbol{\tau}_\theta : \mathbf{d}_\theta^p = \dot{\bar{\epsilon}}_\theta \tau_{\text{eq}\theta} \tag{2.53}$$

and denoting

$$\mathbf{N}_\theta = \mathbf{C} : \mathbf{n}_\theta, \text{ and } A_\theta = \mathbf{n}_\theta : \mathbf{C} : \mathbf{n}_\theta \,, \tag{2.54}$$

one has

$$\dot{\tau}_{\text{eq}\theta} = \mathbf{N}_\theta : \mathbf{d}_\theta - \dot{\bar{\epsilon}}_\theta A_\theta - \frac{\alpha\chi}{\rho C_p}\tau_{\text{eq}\theta}\dot{\bar{\epsilon}}_\theta tr(\mathbf{N}_\theta) \,. \tag{2.55}$$

and

$$\begin{aligned}\Delta\bar{\epsilon} = {} & \dot{\bar{\epsilon}}_t \Delta t + (\theta\Delta t)\frac{\partial\dot{\bar{\epsilon}}}{\partial\bar{\epsilon}}\Delta\bar{\epsilon} + \frac{\partial\dot{\bar{\epsilon}}}{\partial\bar{\tau}_Y}(\theta\Delta t^2) \\ & \cdot\left\{\mathbf{N}_\theta : \mathbf{d}_\theta - \dot{\bar{\epsilon}}_\theta A_\theta - \frac{\alpha\chi}{\rho_0 C_p}\tau_{\text{eq}\theta}\,\dot{\bar{\epsilon}}_\theta tr\big(\mathbf{N}_\theta\big)\right\} \\ & +(\theta\Delta t)\Big(\frac{\partial\dot{\bar{\epsilon}}}{\partial T}\Big)\left(\frac{\chi\tau_{\text{eq}\theta}}{\rho_0 C_p}\right)\Delta\bar{\epsilon}\end{aligned} \tag{2.56}$$

Finally, one can solve this equation to find

$$\begin{aligned}\dot{\bar{\epsilon}}_\theta &= \frac{\Delta\bar{\epsilon}}{\Delta t} \\ &= \frac{\dot{\bar{\epsilon}}_t + (\theta\Delta t)\frac{\partial\dot{\bar{\epsilon}}}{\partial\bar{\tau}_Y}\mathbf{N}_\theta : \mathbf{d}_\theta}{\left(1 - (\theta\Delta t)\frac{\partial\dot{\bar{\epsilon}}}{\partial\bar{\tau}_{Y\theta}} + \frac{\partial\dot{\bar{\epsilon}}}{\partial\bar{\tau}_{Y\theta}}\left(A_\theta + \frac{\alpha\chi}{\rho C_p}\tau_{\text{eq}\theta}tr(\mathbf{N}_\theta)\right) - (\theta\Delta)\frac{\partial\dot{\bar{\epsilon}}}{\partial T}\frac{\chi\tau_{\text{eq}\theta}}{\rho_0 C_p}\right)}\end{aligned} \tag{2.57}$$

Define

$$\begin{aligned}H_\theta = {} & A_\theta + \frac{\alpha\chi}{\rho_0 C_p}\tau_{\text{eq}\theta}tr(\mathbf{N}_\theta) \\ & -\left(\frac{\partial\dot{\bar{\epsilon}}/\partial\bar{\epsilon}}{\partial\dot{\bar{\epsilon}}/\partial\tau_{\text{eq}\theta}} + \frac{\chi\tau_{\text{eq}\theta}}{\rho_0 C_p}\Big(\frac{\partial\dot{\bar{\epsilon}}/\partial T}{\partial\dot{\bar{\epsilon}}/\partial\bar{\epsilon}}\Big)\right),\end{aligned} \tag{2.58}$$

and

$$\xi = (\theta\Delta t)\frac{\partial\dot{\bar{\epsilon}}}{\partial\tau_{\text{eq}\theta}}H_\theta \,. \tag{2.59}$$

One can write

$$\dot{\bar{\epsilon}}_\theta = \frac{\dot{\bar{\epsilon}}_t}{1+\xi} + \frac{\xi}{(1+\xi)H_\theta}\mathbf{N}_\theta : \mathbf{d}_\theta \,. \tag{2.60}$$

The Jaumann rate of the Kirchhoff stress becomes,

$$\begin{aligned}\boldsymbol{\tau}_\theta^{\nabla J} &= \mathbf{C} : \mathbf{d}_\theta - \dot{\bar{\epsilon}}_\theta\mathbf{N}_\theta - 3K\alpha\dot{T}_\theta\mathbf{1}^{(2)} \\ &= \mathbf{C} : \mathbf{d}_\theta - \Big(\frac{\dot{\bar{\epsilon}}_t}{1+\xi} + \frac{\xi}{(1+\xi)H_\theta}\mathbf{N}_\theta : \mathbf{d}_\theta\Big) \\ &\quad\times\Big(\mathbf{N}_\theta + \frac{3K\alpha\chi\tau_{\text{eq}\theta}}{\rho_0 C_p}\mathbf{1}^{(2)}\Big) \,.\end{aligned} \tag{2.61}$$

Temperature is updated by the following operator split scheme. At time $t \in [t_n, t_{n+1}]$ we have the following:

- adiabatic update of rate of temperature at every quadrature point:

$$\dot{T}_n^{gi} = \frac{\chi}{\rho C_p}\bar{\tau}_{Y\theta}\dot{\bar{\epsilon}}$$

- extrapolate the rate of temperature at each particle point ℓ:

$$\dot{T}_n^{\ell a} = \sum_{gi}\frac{\dot{T}_n^{gi}N_\ell(\mathbf{X}_{gi})}{\sum_{gi}N_\ell(\mathbf{X}_{gi})}$$

  where the summation is running through all the quadrature points in the support of the particle ℓ;
- calculate the rate of temperature due to the heat conduction:

$$[\dot{T}_n^{\ell h}] = -[C]^{-1}[H][T_n^\ell]$$

  where the heat capacitance and heat conduction matrices, $[C]$, $[H]$ are defined in Eqs. 2.23 and 2.24;
- update the total temperature:

$$T_{n+1}^\ell = T_n^\ell + (\dot{T}_n^{\ell a} + \dot{T}_n^{\ell h})\Delta t$$

- update (interpolate) the temperature at each quadrature point:

$$T_{n+1}^{gi} = \sum_{i=1}^{\text{np}} N_i(\mathbf{X}_\ell)T_{n+1}^i \,,\ gi = 1, 2, \ldots, gnp \,,$$

  where gnp is the total number of quadrature points.

3 Crack surface approximation and visibility condition

A crucial step in modeling crack propagation in a numerical simulation is how to represent the evolving crack surface and automatically adjust the interpolation field around a growing crack tip. This process is not only a re-interpolation scheme, but also a process to model the material re-configuration.

Belytschko and his co-workers [8,9] have developed a so-called visibility condition that can serve as a criterion to automatically adapt the topological connectivity map among meshfree particles.

There are two shortcomings in the previous meshfree crack surface representation/visibility condition procedure:

(1) crack surface re-construction and representation schemes are complicated. The complexity comes from two sources: the searching algorithm and the re-interpolation algorithm. Because of the technical complexity, any generalization of meshfree crack surface modeling of three-dimensional fracture or ductile fracture becomes a formidable task;
(2) it has been observed that the meshfree shape functions of a re-interpolated field produced by the visibility condition may contain strong discontinuities in meshfree shape functions at certain regions near a crack tip, although we do not know for certain this is indeed a shortcoming.

To simplify the crack surface modeling procedure, we introduce the following crack surface representation and particle splitting algorithm to model crack surface separation.

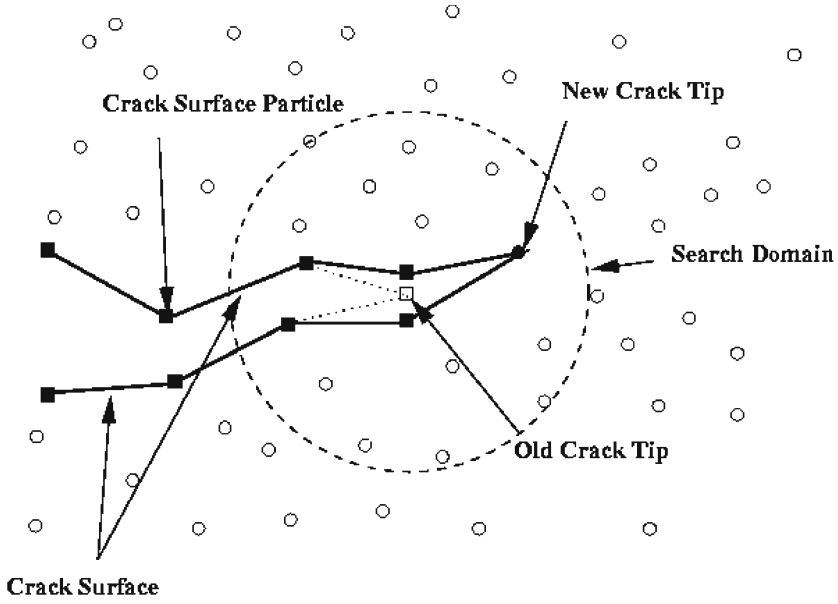

Fig. 1 Illustration of numerical scheme for crack growth

3.1 Crack surface representation and particle splitting algorithm

The two-dimensional crack surface is represented by pairs of piece-wise straight lines as shown in Fig. 1. In Fig. 1, the particles on the crack surface are marked as square black boxes, except at the crack tip, whereas the other meshfree particles are represented as hollow circles. In previous meshfree approaches, when a crack grows, the crack surface is reconstructed by adding new particles. This is not suitable for ductile crack surface modeling, because one has to re-create state variables and re-distribute mass and volume for any newly added particles.

In our approach, a crack tip is always attached to an existing material/interpolation particle. It only moves from one particle to another as shown in Fig. 1.

Assume that the physical criterion to select a new crack tip is available. To find the new crack tip, we first choose a radius R and draw a circle centered at the current crack tip. Then we apply the crack growth criterion to every point inside the circle to decide which point should be the next crack tip, except those points (square boxes) on the crack surfaces, because we do not allow the crack surface become the crack tip again (this may happen in some unusual situations).

Once we select a new crack tip, we split the old crack tip into two points that have the same value of state variables at that particular time. The mass and volume of the two particles are re-assigned according to the following rules, which is called the particle splitting algorithm,

$$\text{Mass}_{\text{new1}} = \frac{\phi_1}{2\pi}\text{Mass}_{\text{old}}, \tag{3.1}$$

$$\text{Mass}_{\text{new2}} = \frac{\phi_2}{2\pi}\text{Mass}_{\text{old}}; \tag{3.2}$$

and

$$\text{Volume}_{\text{new1}} = \frac{\phi_1}{2\pi}\text{Volume}_{\text{old}} \tag{3.3}$$

$$\text{Volume}_{\text{new2}} = \frac{\phi_2}{2\pi}\text{Volume}_{\text{old}} \tag{3.4}$$

The kinematic field variables, such as displacement, velocity, and acceleration of the new particles are assigned as

$$\mathbf{Disp}_{\text{new1}} = \mathbf{Disp}_{\text{old}} + \boldsymbol{\delta} \tag{3.5}$$

$$\mathbf{Disp}_{\text{new2}} = \mathbf{Disp}_{\text{old}} - \boldsymbol{\delta} \tag{3.6}$$

$$\mathbf{Vel}_{\text{new1}} = \mathbf{Vel}_{\text{old}} \tag{3.7}$$

$$\mathbf{Vel}_{\text{new2}} = \mathbf{Vel}_{\text{old}} \tag{3.8}$$

$$\mathbf{Acc}_{\text{new1}} = 0.0d0$$

$$\mathbf{Acc}_{\text{new2}} = 0.0d0 \tag{3.9}$$

where $\boldsymbol{\delta}$ is a vector whose length $|\boldsymbol{\delta}| << 1$. It serves the purpose of making a physical distinction between the two new particles once they are separated.

The state variables are re-assigned as

$$\text{Temp}_{\text{new1}} = \text{Temp}_{\text{old}} \tag{3.10}$$

$$\text{Temp}_{new2} = \text{Temp}_{\text{old}} \tag{3.11}$$

$$\text{Damage}_{\text{new1}} = \text{Damage}_{\text{old}} \tag{3.12}$$

$$\text{Damage}_{\text{new2}} = \text{Damage}_{\text{old}} \tag{3.13}$$

This process is illustrated in Fig. 2, in which the point $(X_{\text{tip}}, Y_{\text{tip}})$ is the new crack tip, and the old crack tip is split into two particles, $(X_{\text{new1}}, Y_{\text{new1}})$ and $(X_{\text{new2}}, Y_{\text{new2}})$. A pair

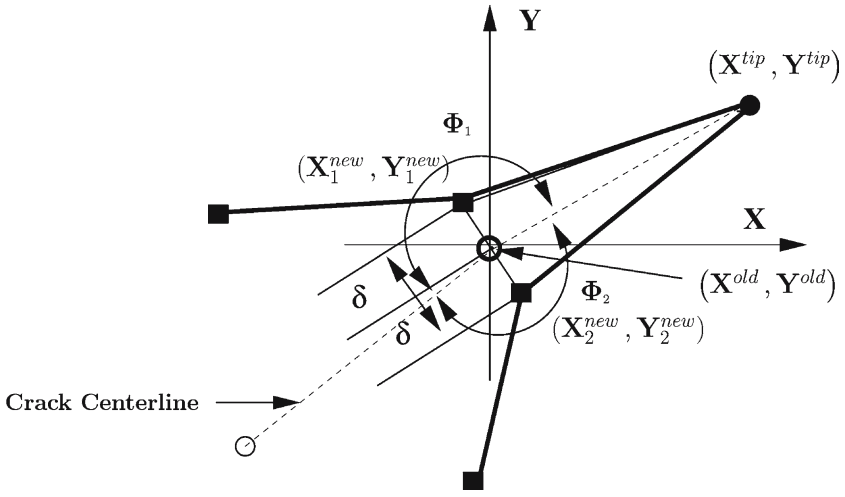

Fig. 2 Meshfree particle splitting algorithm

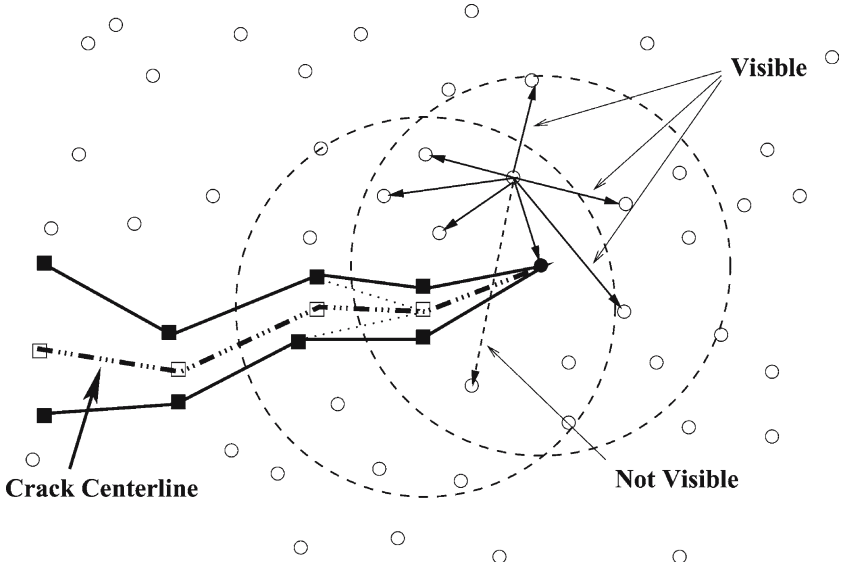

Fig. 3 Visibility condition in 2D

of straight lines connect $(X_{\text{new1}}, Y_{\text{new1}})$ and $(X_{\text{new2}}, Y_{\text{new2}})$ with the new crack tip, $(X_{\text{tip}}, Y_{\text{tip}})$.

3.2 Parametric visibility condition

Meshfree interpolation relies on a local connectivity map to associate one particle with its neighboring particles.

To model crack propagation, one has to develop a numerical algorithm that can automatically modify the local connectivity map and simulate a running crack without user interference.

The parametric visibility condition used in this study is developed by Li & Simonsen [34], which can be used to modify the local meshfree connectivity map to reflect geometric change of domain due to crack growth.

The visibility condition used in this study is illustrated in Fig. 3. Figuratively speaking, a crack may be viewed as an opaque wall. A material point on one side of the wall can not "see" the material points on the other side of the wall. This principle is called the "visibility condition". To determine

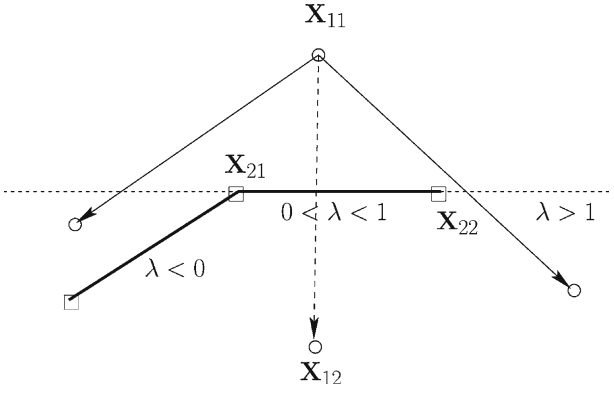

Fig. 4 Parametric visibility conditions

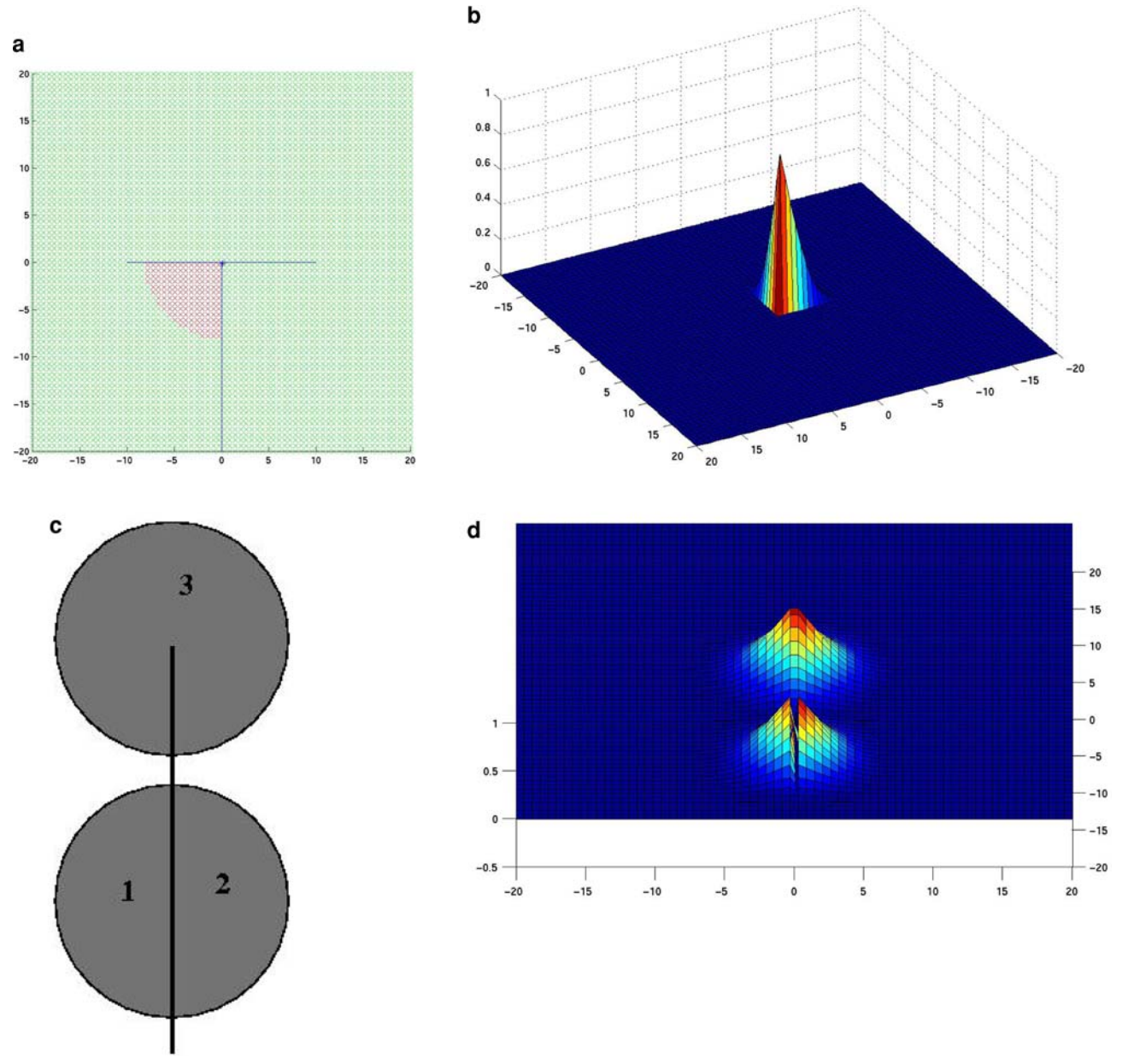

Fig. 5 Meshfree shape function along crack surfaces (I)

whether or not two material points are separated by a crack segment, one can check whether or not the line segment connecting two material points intercept the crack path segment. This crack path segment is shown as a dashed line in Fig. 3.

Since crack growth is incremental, one only needs to check and to modify a limited number of particles in the current crack tip area, which is defined as the union of two circles centered at the current crack tip and next crack tip (see Fig. 3). To modify the meshfree connectivity map, one only needs to check the visibility condition inside the union of two circles, $\mathcal{C} = \mathcal{C}_1 \bigcup \mathcal{C}_2$. This process is named the "parametric visibility condition".

Suppose that we want to modify the connectivity relation between particle $(X_{11}, Y_{11}) \in \mathcal{C}$ and the rest of the particles inside $\mathcal{C}$. We denote an arbitrary point inside $\mathcal{C}$ as (X_{12}, Y_{12}) and two crack tips (old and new) as (X_{21}, Y_{21}) and (X_{22}, Y_{22}).

The parametric equations of the straight line that connects points (X_{11}, Y_{11}) and (X_{12}, Y_{12}) are

$$\begin{cases} X = X_{11} + \lambda_1 \Delta X_1 \\ Y = Y_{11} + \lambda_1 \Delta Y_1 \end{cases} \tag{3.14}$$

where λ_1 is the parametric variable and

$$\Delta X_1 := X_{12} - X_{11} \tag{3.15}$$

$$\Delta Y_1 := Y_{12} - Y_{11} \tag{3.16}$$

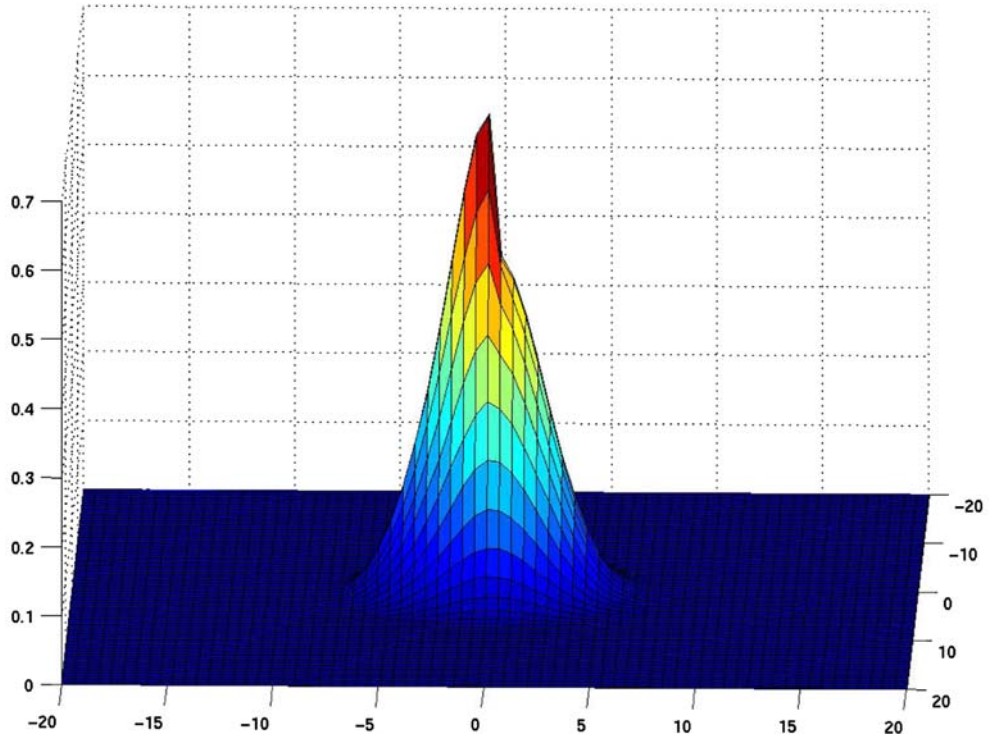

Fig. 6 Strong discontinuity of a meshfree shape function at a crack tip

On the other hand, the parametric equations for the straight line that connects two crack tips are,

$$\begin{cases} X = X_{21} + \lambda_2 \Delta X_2 \\ Y = Y_{21} + \lambda_2 \Delta Y_2 \end{cases} \tag{3.17}$$

where λ_2 is the parametric variable and

$$\Delta X_2 := X_{22} - X_{21} \tag{3.18}$$

$$\Delta Y_2 := Y_{22} - Y_{21} \tag{3.19}$$

If the two line segments intersect each other, one can equate Eqs. (3.14) and (3.17), and solve for λ_1 and λ_2,

$$\begin{bmatrix} \lambda_1 \\ \lambda_2 \end{bmatrix} = \frac{1}{(\Delta X_1 \Delta Y_2 - \Delta X_2 \Delta Y_1)} \times \begin{bmatrix} \Delta Y_2 (X_{21} - X_{11}) - \Delta X_2 (Y_{21} - Y_{11}) \\ \Delta Y_1 (X_{21} - X_{11}) - \Delta X_1 (Y_{21} - Y_{11}) \end{bmatrix} \tag{3.20}$$

If the two line segments intersect each other, the following **parametric visibility conditions** have to be satisfied,

$$0 < \lambda_1 < 1, \quad \text{and} \quad 0 < \lambda_2 < 1 \ . \tag{3.21}$$

These parametric visibility conditions are illustrated in Fig. 4. If both parametric visibility conditions are met, then the line segment between two arbitrary points inside $\mathcal{C}$ will intersect the newly formed crack surfaces and hence one should disconnect the connection between these two points. This case is depicted by the dashed line between particles in Fig. 4. In other words, either point should be removed from the other point's connectivity map, and it then ensures that there is no non-physical cross-crack interpolation.

In the following, a few artificial examples are shown to display the meshfree shape functions that are constructed at the crack surface via the particle splitting algorithm, connectivity modification, and parametric visibility condition.

Figure 5 a, b, show a meshfree shape function whose support has been reduced up to 3/4 by two orthogonally running cracks. Figure 5 c, d, show a meshfree function that has been cut by a crack into two parts and another meshfree shape function right at the crack tip.

It should be mentioned that the shape function at the crack tip generated using the visibility condition may have

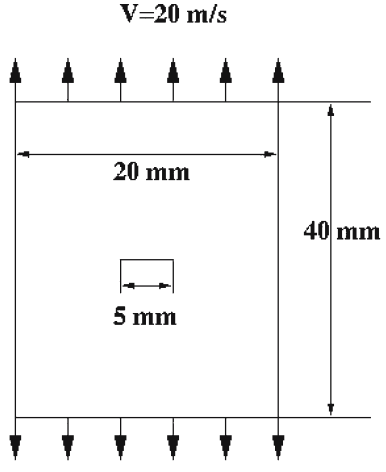

Fig. 7 Dimensions of the tension test specimen

a singular value at certain points close to the crack tip, see Fig. 6. However, as shown by Krysl and Belytshko [16], as the average particle spacing, h, approaches zero, such discontinuities will disappear and the erroneous energy due to the artifical discontinuity will disappear as well.

4 Numerical examples

Instead of using the weak formulation (2.1), the actual meshfree simulation is based on the following total Lagrangian variational (weak) formulation,

$$\int_{\Omega_X} \rho_0 \ddot{u}_i \delta u_i \, \mathrm{d}\Omega_X + \int_{\Omega_X} P_{iJ} \delta F^T_{iJ} \, \mathrm{d}\Omega_X - \int_{\Omega_X} \rho_0 B_i \delta u_i \, \mathrm{d}\Omega_X - \int_{\Gamma^T_X} T^0_i \delta u_i \, \mathrm{d}\Gamma = 0 \, . \tag{4.1}$$

where the T^0_i are the components of a prescribed traction force on the traction boundary, Γ^T_X, and $\mathbf{P}$ denote the nominal stress tensor, which is the transpose of the first Piola-Kirchhoff stress, and it can be related to the Kirchhoff stress tensor by the expression, $\boldsymbol{\tau} = \mathbf{P}\mathbf{F}^{\mathrm{T}}$, ρ_0 is the density in the reference configuration, and $\mathbf{B} = B_i \mathbf{e}_i$ is the body force per unit mass.

The general boundary conditions in the reference configuration are stated as

$$\mathbf{n} \cdot \mathbf{P} = \mathbf{T}^0, \quad \forall \mathbf{X} \in \Gamma^{\mathrm{T}}_X \tag{4.2}$$

$$\mathbf{u} = \bar{\mathbf{u}}, \quad \forall \, \mathbf{X} \in \Gamma^u_X \tag{4.3}$$

It should be noted that the meshfree interpolant used is not able to represent boundary data via boundary value interpolation. Therefore, an extra term appears in the weak form (4.1)

$$\int_{\Gamma^u_X} \mathbf{T} \cdot \delta \mathbf{u} \, \mathrm{d}\Gamma_X \tag{4.4}$$

because $\delta \mathbf{u} \neq \mathbf{0}, \ \forall \, \mathbf{X} \in \Gamma^u_X$. For further details on how to estimate this term and enforce the essential conditions, the readers are referred to Li and Liu [18].

To test the meshfree algorithm, we have conducted the following numerical experiment simulating ductile fracture of a plate (see Fig. 7). We further assume that the specimen is under a plane strain condition. As shown in Fig. 7, a rectangular specimen has a center crack embedded in the middle of the plate, which has initial length 5.0 mm. Velocity boundary conditions are prescribed at both ends of the plate, so it renders the plate under uniaxial tension loading.

The following material parameters are used in the Johnson-Cook model:

$$\begin{aligned} &E = 211 \text{ GPa} \\ &\rho = 7800 \text{ kg/m}^3 \\ &\nu = 0.3 \\ &A = 455.0 \times 10^6, \quad B = 237.0 \times 10^6, \\ &C = 6.0 \times 10^{-3}, \quad N = 0.370, \\ &m = 1.00, \quad T_{\text{melt}} = 1500.0, \quad T_{\text{room}} = T_0 = 300.0, \end{aligned} \tag{4.5}$$

The fracture criteria that we used is a damage based criterion. Initially, we set up a critical damage value as the fracture threshold. In this example, that threshold is chosen as $damage_{cr} = 0.80$. At each time step, we evaluate the damage value of each particle in the neighborhood of the crack tip (the circle in Fig. 1). Once the damage value of a particle exceeds $damage_{cr}$, we declare the particle as the new crack tip. If the damage value of two or more particles exceeds $damage_{cr}$ at the same time step, this may signal crack bifurcation.

In the current simulation, we simply choose the particle that has the largest damage value among all the other particles whose damage value exceed $damage_{cr}$ as the new crack tip. Once the linear equation of the line segment connecting the old and the new crack tips is established, one can apply the proposed parametric visibility condition to modify the connectivity map and hence to construct the new traction-free crack surface. The numerical results presented in Figs. 7, 8, and 9 are obtained based on the material parameters listed in Table 1. In the actual meshfree discretization, there are 5,164 particles used in interpolation, and 20, 000 quadrature points used in numerical integration.

In Fig. 8, the normal stress component σ_{22} and the shear stress component σ_{12} are displayed at various time instances during the fast crack propagation process. One may find that there are zero or low stress regions along the growing crack surfaces, i.e., the blue colour regions. This indicates that the crack surfaces are traction free surfaces, which indirectly verifies the fact that the crack surfaces constructed by the visibility condition and meshfree crack surface re-construction process are successful. Moreover, it is interesting to note that in Fig. 8 e, f, g and h, one can find that across the growing crack surfaces the shear stress, σ_{12}, changes its sign and its distribution is anti-symmetric about the x_2 axis. These facts are shown by the fact that when $x < 0$ there is a blue region (lower shear stress value) below the crack surface, and there

Table 1 Material parameters used in the computer simulations

Parameter	Value	Definition
$\dot{\epsilon_0}$	$1 \times 10^4 \text{ s}^{-1}$	Reference strain rate
m	70	Rate sensitivity parameter
σ_0	200 MPa	Yield stress
ϵ_0	σ_0/E	
N	0.01	Strain hardening exponent
T_0	293 K	Reference temperature
κ	500 K	Thermal softening parameter
E	200 GPa	Young's modulus
ν	0.3	Poisson's ratio
ρ_0	7830 kg m^{-3}	Mass density
C_p	448 J (kg $\cdot$ K)$^{-1}$	Specific heat
α	11.2×10^{-6} K^{-1}	Coefficient of thermal expansion
χ	0.9	The fraction of plastic work converted to heat
D_1	0.005	Damage parameter
D_2	30.500	Damage parameter
D_3	-2.120	Damage parameter
D_4	0.002	Damage parameter
D_5	1.600	Damage parameter

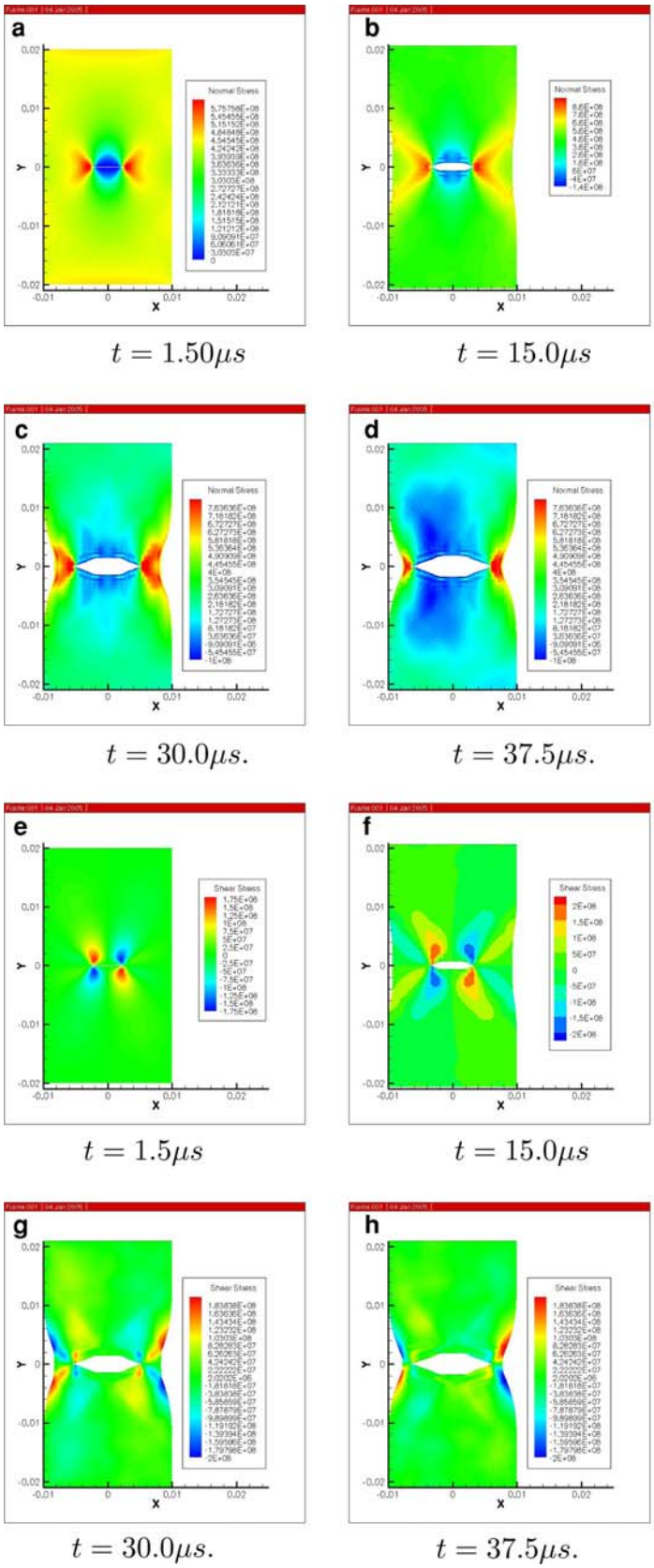

Fig. 8 Contours of normal stress σ_{22} (a), (b), (c), (d) and the contours of shear stress σ_{12} (e), (f), (g), and (h)

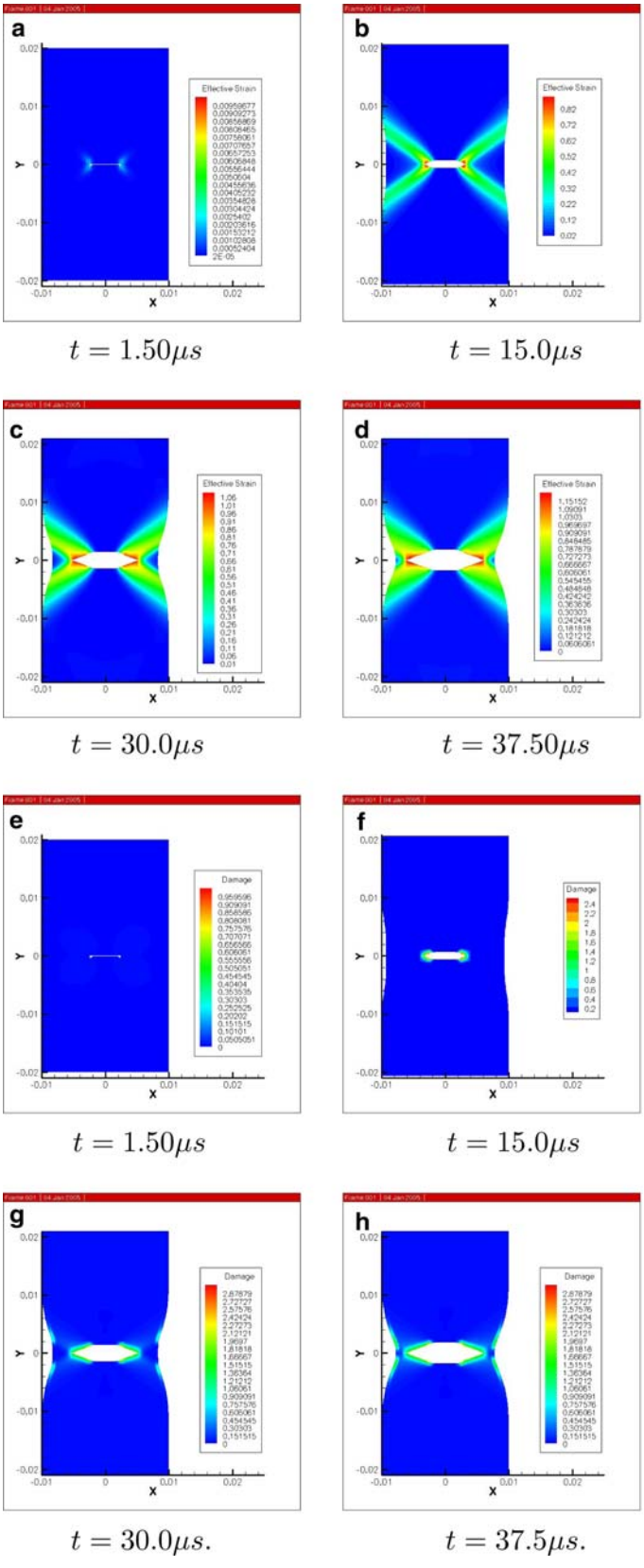

Fig. 9 Effective strain contours: (a), (b), (c), (d) and damage contours: (e), (f), (g), (h)

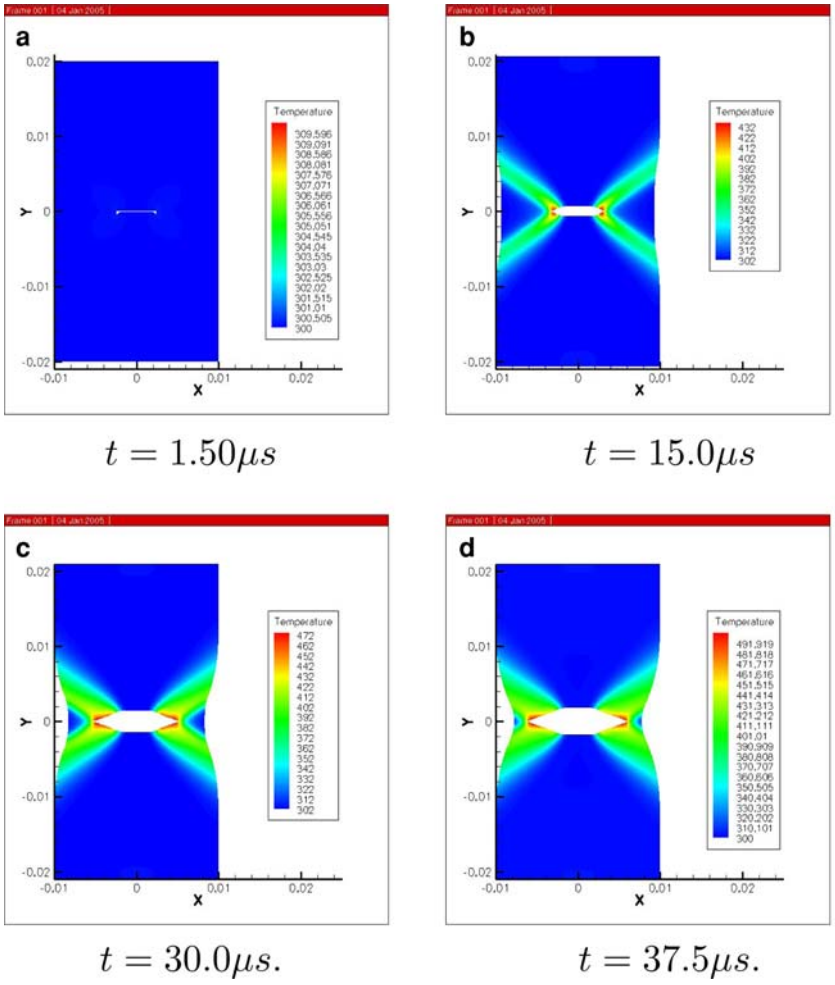

Fig. 10 Temperature contours (a), (b), (c), and (d)

is a red region (higher shear stress value) above the crack surface; and when $x > 0$ there is a red region (high shear stress value) below the crack surface, and there is a blue region (low shear stress value) above the crack surface.

Temperature profiles are displayed in Fig. 10. One may observe that the temperature profile is very similar to the effective strain profiles. This is because the temperature rise is driven by heat generation during plastic yielding and plastic deformation. The plastic deformations are mainly confined to regions that form a 45° angle from the initial crack orientation. On the other hand, heat induced thermal-softening leads to strain localization. Therefore, high temperature regions are also strain localization regions or shear-band regions. Adiabatic shear-bands can be observed both in the temperature profile as well as the effective strain rate profile, and as time goes by, when the heat conduction effect activates, the width of the shear band increases.

By carefully observing the temperature profiles, one may find that the heat generated has caused a large temperature rise. The initial room temperature is fixed at $T_0 = 300\,\mathrm{K}$. At the end of the simulation, the maximum temperature in a specimen can increase to as high as 500 K, which is an increase of two thirds of the initial room temperature.

Zooming in to the crack region, we can observe the crack surface morphology. Figure 11 shows the normal stress distribution, σ_{22}, and effective strain distribution around a crack region.

A careful observation of Fig. 11 reveals some important features of ductile fracture. As noted earlier, there is a growing blue region that surrounds the the crack surface, which indicates that there is a growing region with zero or very low normal stress value around crack surfaces. This demonstrates that the automatically adjusted meshfree surface interpolation works, and the newly formed crack surface is indeed a traction-free surface, or almost traction-free. This indirectly proves that the crack growth algorithm implemented is working, and it is validated by the manifestation of correct physical responses around the propagating crack tip. Second, for certain damage model parameters, the ductile crack surface shows irregular features. The strain and stress contours shown in Fig. 11 are obtained with the following damage parameters:

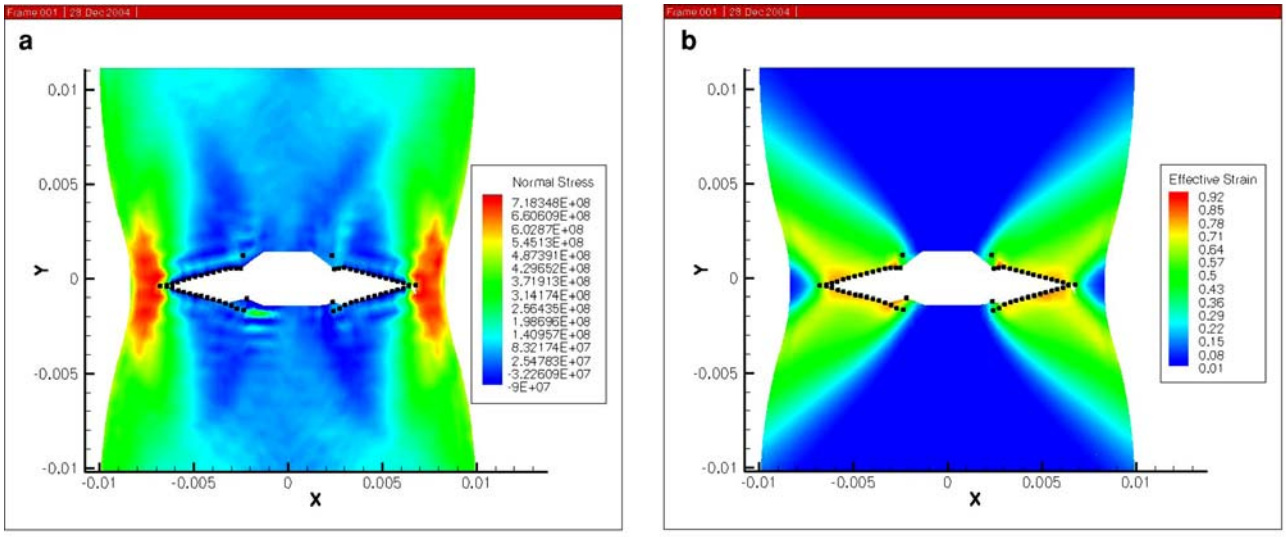

Fig. 11 Crack surface morphology **(a)** σ_{22} contour, **(b)** effective strain contour

$D_1 = 0.005$, $D_2 = 3.00$, $D_3 = -2.120$, $D_4 = 0.002$, and $D_5 = 0.610$.

Note that the black circle dots in Fig. 11 represent the particles on the crack surfaces, or the evolving crack surfaces are constructed by those particles.

Rough crack surfaces are a trademark of ductile fracture [28–30]. To the best of the authors' knowledge, this unique feature of ductile fracture has been difficult to capture in numerical simulations. Third, visible necking due to strain softening and material instability can be found Figs. 7, 8, 9 and 10.

5 Discussions

There are a few important technical issues worth discussing. First, by accounting for thermo-mechanical effects, in particular, heat conduction, the Johnson-Cook model based constitutive relations are well regularized, and are numerically stable. By comparing to the previous simulations by the same group of authors [24], which adopted the Gurson-Tvergarrd-Needleman (GTN) damage model, the Johnson-Cook model provides an intrinsic length scale, and it leads to finite shear band width and stable numerical computations.

Second, by using a meshfree simulation alone, one can not eliminate mesh sensitivity, in this case, the particle distribution dependency. To a certain extent, we believe that the numerical result presented in this paper may alter to a certain degree when different particle distributions are employed. Nevertheless, we also believe that the main feature captured in this study will remain, such as large crack opening and rough crack surface morphology, which is due to the physics of the problem. In fact, the initial particle distribution used in the simulation is almost uniform throughout the domain. Particles are placed in a square pattern and they are symmetrically located relative to the mesh generator's numerical precision, and there may be a small random error distribution due to round-off in floating point arithmetic.

Acknowledgements This work is made possible by a National Science Foundation Career Award to Professor Shaofan Li (Grant No. CMS-0239130 to University of California at Berkeley), which is greatly appreciated. The authors would like to thank Mr. Xiaohu Liu for his help generating meshfree shape functions with discontinuities.

References

1. Armero F, Simo JC (1992) A new unconditionally stable fractional step method for non-linear coupled thermomechanical problems. Int J for Numer Meth Eng 35:737–766
2. Armero F, Simo JC (1993) A priori stability estimates and unconditionally stable product formula algorithms for nonlinear coupled thermoplasticity. Int J Plasticity 9:749–782
3. Batra RC, Chen L (2001) Effect of viscoplastic relations on the instability strain, shear band initation strain, the strain corresponding to the minimum shear band spacing and the band width in a thermoviscoplastic material. Int J Plasticity 17:1465–1489
4. Belytschko T, Lu YY, Gu L (1994a) Element Free Galerkin Methods. Int J Numer Meth Eng 37:229–256
5. Belytschko T, Lu YY, Gu L (1994b) Fracture and Crack Growth by Element-free Galerkin Methods. Model Simul Sci Comput Eng 2:519–534
6. Belytschko T, Lu YY, Gu L (1995a) Element-free Galerkin Methods for Static and Dynamic Fracture. Int J Solids Struct 32:2547–2570
7. Belytschko T, Lu YY, Gu L (1995b) Crack propagation by Element-free Galerkin Methods. Eng Fracture Mech 51:295–315
8. Belytschko T, Krongauz Y, Organ D, Fleming M, Krysl P (1996a) Meshless methods: An Overview and Recent Developments. Comput Meth Appl Mech Eng 139:3–48
9. Belytschko T, Krongauz Y, Fleming M, Organ D, Liu WK (1996b) Smoothing and accelerated computations in the element free Galerkin method. J Comput Appl Math 74:111–126

10. Belytschko T, Tabbara M (1997) Dynamic Fracture Using Element-free Galerkin Methods. J Comput Appl Math 39:923–938
11. Daux C, Moes N, Dolbow J, Sukumar N, Belytschko T (2000) Arbitrary branched and intersecting cracks with the extended finite element method. Int J Numer Meth 48:1741–1760
12. Dolbow J, Moës N, Belytschko T (2000) Discontinuous enrichment in finite elements with a partition of unity method. Finite Elem Anal Design 36:235–260
13. Fleming M, Chu YA, Moran B, Belytschko T (1997) Enriched element-free Galerkin methods for crack tip fields. Int J Numer Meth Eng 40:1483–1504
14. Johnson GR, Cook WH (1983) A constitutive model and data for metals subjected to large strains, high strain rates and high temperature. In: Proceedings of the 7th international symposium on ballistics, The Hague, The Netherlands, pp 1–7
15. Johnson GR, Cook WH (1985) Fracture Characteristics of Three Metals Subjected to Various Strains, Strain Rates, Temperatures and Pressures. Eng Fract 21:31–48
16. Krysl P, Belytschko T (1996) Element-free Galerkin method: convergence of the continuous and discontinuous shape function. Comput Meth Appl Mech Eng 148:257–277
17. Krysl P, Belytschko T (1999) The element free Galerkin method for dynamic propagation of arbitrary 3-D cracks. Int J Solids Struct 44:767–800
18. Li S, Liu WK (2000) Numerical Simulations of Strain Localization in Inelastic Solids Using Meshfree Methods. Int J Numer Meth Eng 48:1285–1309
19. Lu YY, Belytschko T, Tabbara M (1995) Element-free Galerkin Method for wave Propagation and Dynamic Fracture. Comput Meth Appl Mech Eng 126:131–153
20. Gurson AL (1977) Continuum theory of ductile rupture by void nucleation and growth: Part I yield criteria and flow rules for porous ductile materials. J Eng Materials Tech 99:2–15
21. Ortiz M, Pandolfi A (1999) Finite-deformation irreversible cohesive elements for three-dimensional crack-propagation analysis. Int J Numer Meth Eng 44:1267–1282
22. Peirce D, Shih CF, Needleman A (1984) A tangent modulus method for the rate dependent solids. Comput Struct 18:168–173
23. Rashid YR (1968) Analysis of prestressed concrete vessels. Nuclear Eng Design 7:334–355
24. Simonsen BC, Li S (2004) Meshfree modeling of ductile fracture. Int J Numer Meth Eng 60:1425–1450
25. Stolarska M, Chopp DL, Moes N, Belytschko T (2001) Modelling crack growth by level sets in the extended finite element method. Int J Numer Meth Eng 51:943–960
26. Ventura G, Xu JX, Belytschko T (2002) A vector level set method and new discontinuity approximations for crack growth by EFG. Int J Numer Meth Eng 54:923–944
27. Wawrzynek PA, Ingraffea AR (1987) Interactive finite element analysis of fracture processes: an integrated approach. Theor Appl Fract Mech 8:137–150
28. Xia L, Shih CF, Hutchinson JW (1995a) Computational approach to ductile crack growth under large scale yielding conditions. J Mech Phys Solids 43:389–413
29. Xia L, Shih CF (1995b) Ductile crack growth –II. Void nucleation and geometry effects on macroscopic fracture behavior. J Mech Phys Solids 43:1953–1981
30. Xia L, Shih CF, Hutchinson (1995c) A computational approach to ductile crack growth under large scale yielding conditions. J Mech Phys Solids 43:389–413
31. Xu P, Needleman A (1994) Numerical simulations of fast crack growth in brittle solids. J Mech Phys Solids 42:1397–1434
32. Zhou M, Rosakis AJ, Ravichandran G (1996a) Dynamically Propagating Shear Bands in Impact-loaded Prenotched Plates—I Experimental Investigations of Temperature Signatures and Propagation Speed. J Mech Phys Solids 44:981–1006
33. Zhou M, Ravichandran G, Rosakis AJ (1996b) Dynamically Propagating Shear Bands in Impact-loaded Prenotched Plates—II Numerical Simulations. J Mech Phys Solids 44:1007–1032
34. Li S, Simonsen BC (2005) Meshfree simulation of ductile crack propagations. Int. J. for Comput. Methods in Eng. Sci. and Mechanics 6:1–19